

# LISA as a probe of pre-big-bang physics: a nested sampling analysis

Xoán Vilas Currás <sup>a</sup>, Gianluca Calcagni <sup>b,\*</sup>

<sup>a</sup>Departamento de Astrofísica, Universidad de La Laguna, Avenida Astrofísico Francisco Sánchez, 38200 Tenerife, Spain

<sup>b</sup>Instituto de Estructura de la Materia, CSIC, Serrano 121, 28006 Madrid, Spain

E-mail: [xoan.cosmo@gmail.com](mailto:xoan.cosmo@gmail.com), [g.calcagni@csic.es](mailto:g.calcagni@csic.es)

**Abstract.** Using a nested sampling analysis, we study the gravitational-wave background (GWB) predicted by pre-big-bang cosmology, both in its minimal and non-minimal version. Within the LISA sensitivity range, the GWB signal is a flat or a broken power law, parametrized by four fundamental quantities: the Hubble parameter at the curvature bounce  $H_1$ , the axion mass  $m$ , the initial amplitude of the axion field  $\sigma_i$  and the exponent  $\beta$  governing the high-energy growth of the dilaton and the dynamics of the internal dimensions. We determine the posterior distributions of these parameters based on how LISA would detect such signal. Including the galactic and extra-galactic foregrounds in the analysis, the most stringent constraints on  $H_1$ ,  $\sigma_i$  and  $\beta$  are obtained when the signal exhibits a left-bend feature, while for  $m$  this happens for a right-bend feature. Relative uncertainties reach  $\Delta H_1/H_1$ ,  $\Delta m/m \sim 18\%$  at 68% confidence level under favourable conditions. LISA will thus be capable of placing significant constraints on the pre-big-bang model, potentially providing empirical hints of string theory in the case of detection.

**Keywords:** Primordial gravitational waves (theory), Gravitational waves in GR and beyond: theory, Quantum gravity phenomenology, String theory and cosmology.

---

\*Corresponding author.

---

## Contents

<b>1</b>	<b>Introduction</b>	<b>1</b>
<b>2</b>	<b>Pre-big-bang cosmology</b>	<b>2</b>
<b>3</b>	<b>Parameter space</b>	<b>6</b>
<b>4</b>	<b>Methodology and results</b>	<b>7</b>
<b>5</b>	<b>Discussion</b>	<b>13</b>
<b>6</b>	<b>Conclusions</b>	<b>13</b>
<b>A</b>	<b>Derivation of (2.6)</b>	<b>15</b>
<b>B</b>	<b>Derivation of (3.5)</b>	<b>16</b>

---

## 1 Introduction

Gravitational waves (GWs) are a recent discovery [1] that is rapidly populating our previously blind view of the cosmos with sources [2, 3] and revolutionizing our approach to astrophysics and cosmology. Each advance in GW detection has so far confirmed the validity of Einstein’s classical theory of general relativity (GR) [4–7]. However, attempting to describe our observable universe entirely with a classical theory may lead to an incomplete description or explanation of phenomena where quantum mechanics plays a major role. GWs offer a unique opportunity to test not only GR but also its modifications beyond the classical level. In particular, primordial GWs were generated before photon decoupling and can provide valuable information about epochs prior to the formation of the cosmic microwave background, since unlike light they interact very weakly with matter and thus travel almost unimpeded across the universe.

GWs can be generated in two main ways: by astrophysical sources (galactic and extragalactic black-hole, neutron-star and white-dwarf binaries) or by cosmological sources (inflation, phase transitions, cosmic strings and primordial black holes) [8–13]. In the first case, GWs can arrive either from individual sources or as a stochastic superposition of many signals forming gravitational-wave background (GWB) [14–16]. In the second case, GWs manifest themselves primarily as a GWB.

Among the cosmological mechanisms, one case of particular interest is the GWs produced around the big bang itself. This event marking the beginning of Everything arises from extrapolating GR to the origin of time. However, at epochs close to  $t = 0$  the classical theory breaks down and quantum effects become as important as, or even dominate over, the classical gravitational force. Therefore, to properly describe the origin of the universe, a theory of quantum gravity might be required. Among many other candidates capable of incorporating quantum mechanics and gravity [17–19], string theory has been employed to address this issue. And, among many other models of string cosmology, one in particular has the potential of leaving an imprint in GW physics: the pre-big-bang model of the early universe [20–30].

According to this paradigm, a consequence of T-duality [31] is that the big bang does not represent the true origin of time but, rather, a moment of maximum curvature and energy density, implying the existence of a preceding phase from  $t = -\infty$  to  $t = 0$ , known as the pre-big-bang era. If this model is correct, then GWs can be generated during the pre-big-bang phase and leave a relic in the form of a cosmological GWB. The existence of a GWB background has already been confirmed by observations in a relatively narrow frequency range [32–37] but the current challenge lies not only in scrutinizing its possible astrophysical origin and identifying individual contributions from different sources, but also in spanning a larger frequency range in search for a continuation of this signal or for new ones of different origin. Accomplishing this highly demanding task requires high-resolution measurements across various frequency bands, which are expected to be provided by future GW detectors such as the Laser Interferometer Space Antenna (LISA) [9–12] and the Einstein Telescope [8, 13]. The bulk of the signal of the pre-big-bang GWB should fall within the sensitivity frequency window of these two observatories in particular [28]. In this publication, the GWB of the model was plotted against the sensitivity curves of LISA and Einstein Telescope but little was said about the constraints these detectors will be able to place upon the pre-big-bang scenario.

Until LISA and the Einstein Telescope become operational in the 2030s, we must rely on numerical simulations to “test” theoretical models. In this work, we build upon the framework developed in [29] to recast the pre-big-bang GWB in terms of the parameter space made of physical constants. Then, we naturally continue the analysis of [28] and apply a LISA-specialized Python package, `SGWBinner` [38–40], to compute posterior distributions for various test cases, thus preparing the ground for future detection efforts with LISA.

The conclusions of this work indicate that LISA has the potential to place significant constraints on the model. The latter would emerge as a compelling high-energy candidate, although it would not constitute a confirmation of the model since other, more conventional early-universe scenarios can produce a similar signal. In this case, additional and complementary multi-messenger observations would be needed to disentangle this degeneracy. Conversely, if LISA set bounds incompatible with the theoretically viable parameter space, the model in its present form would be ruled out. A third and, for obvious reasons, less attractive possibility is that the parameter space were constrained to a region where the signal is undetectable by LISA, thus relegating the model to a minor spectator to be “further investigated in the future.”

This paper is organized into the following sections: a brief review of the pre-big-bang cosmology model in section 2, a description of the parameter space used in our analysis in section 3, the methodology and results obtained using `SGWBinner` in section 4 and their discussion in section 5. Conclusions are presented in section 6. The derivation of some formulæ can be found in the appendices. We work in natural units  $\hbar = 1 = c$  and  $M_{\text{Pl}} = 1$ .

## 2 Pre-big-bang cosmology

The pre-big-bang model [20] is an attempt to embed a description of the early Universe in string theory. Here, the role of the inflation field is played by the dilaton, a fundamental scalar field coupled to gravity whose axionic partner is the Kalb–Ramond axion. The big bang singularity is replaced by a state of maximal curvature and energy density. The Universe starts in the perturbative string vacuum with an zero curvature and string coupling  $g_s$ ; quantum perturbations trigger the dilaton and axion dynamics and the curvature begins to grow with

the dilaton, until it reaches a maximum. After this stage, the Kalb–Ramond axion decays, leading to a conventional reheating phase.

Following the analyses in [28, 29], this process is characterized by five different phases:

1. Low-energy string:  $\xi \propto (-\tau)^{1/2}$ ,  $\tau < -\tau_s$ .
2. De Sitter-like evolution:  $\xi \propto (-\tau)^{\beta-1}$ ,  $-\tau_s < \tau < -\tau_1$ .
3. Radiation-dominated evolution  $\xi \propto \tau$ ,  $-\tau_1 < \tau < \tau_\sigma$ .
4. Matter-dominated evolution  $\xi \propto \tau^2$ ,  $\tau_\sigma < \tau < \tau_d$ .
5. Radiation-dominated evolution  $\xi \propto \tau$ ,  $\tau > \tau_d$ .

Here  $\xi$  describes the so-called “pump field” that governs the dynamics of the perturbation modes in the given background and  $\tau$  is conformal time.  $-\tau_s$  marks the transition from a low-energy initial phase to a possible late-time attractor;  $-\tau_1$  marks the time scale of the curvature bounce;  $\tau_\sigma$  marks the beginning of a dust-like phase dominated by axion oscillations; and  $\tau_d$  marks the decay of the axion, associated with conventional reheating. The parameter  $\beta$  describes the high-energy growth of the dilaton and the dynamics of the internal dimensions.

Each conformal time scale can be conveniently replaced by its corresponding curvature scale, denoted by  $H_s$ ,  $H_1$ ,  $H_\sigma$  and  $H_d$ . It is convenient to define the wave-number  $k$  associated with primordial GW modes, focusing on the interval  $k_0 \leq k \leq k_1$ , where  $k_0 \equiv \tau_0^{-1}$  is the minimal wave-number corresponding to the largest observable scale today and  $k_1 \equiv \tau_1^{-1}$  denotes the maximal frequency that exited the horizon at the end of the pre–big-bang inflationary phase, meaning that they are inside the present Hubble horizon. This wave-number can be converted into the corresponding proper frequency  $f$  via the relation  $\omega(\tau) = k/a(\tau)$ , where  $a(\tau)$  is the scale factor at conformal time  $\tau$  and  $\omega = 2\pi f$ . Lastly, the following dimensionless parameters are often used in the literature:

$$z_s := \frac{\tau_s}{\tau_1} = \frac{k_1}{k_s}, \quad z_\sigma := \frac{\tau_\sigma}{\tau_1} = \frac{k_1}{k_\sigma}, \quad z_d := \frac{\tau_d}{\tau_1} = \frac{k_1}{k_d}, \quad (2.1)$$

which control the extension of the pre-bouncing high curvature regime and of the two post-bouncing phases.

There are two pump fields: one for scalar perturbations and another for tensor perturbations. Two scenarios are possible: a *minimal* one where the string spectrum increases and S-duality is preserved [28] and a *non-minimal* one where either or both conditions (increasing spectrum and S-duality) are broken [29, 30]. Both scenarios yield the same parametric solutions within each cosmological phase and, consequently, produce the same form of GWB. The primary distinction lies in the extension of the parameter space of the model, which will be discussed in detail in the following sections.

In terms of the characteristic frequencies  $f_1$ ,  $f_\sigma$ ,  $f_d$  and  $f_s$ , the GWB generated in each

phase takes the asymptotic form

$$\Omega_{\text{GW}}(f) = \begin{cases} \Omega_{\text{PBB}} \left( \frac{f}{f_1} \right)^{3-|3-2\beta|}, & f_\sigma \lesssim f \lesssim f_1 \\ \Omega_{\text{GW}}(f_1) \left( \frac{f_\sigma}{f_1} \right)^{3-|3-2\beta|} \left( \frac{f}{f_\sigma} \right)^{1-|3-2\beta|}, & f_d \lesssim f \lesssim f_\sigma \\ \Omega_{\text{GW}}(f_\sigma) \left( \frac{f_d}{f_\sigma} \right)^{1-|3-2\beta|} \left( \frac{f}{f_d} \right)^{3-|3-2\beta|}, & f_s \lesssim f \lesssim f_d \\ \Omega_{\text{GW}}(f_d) \left( \frac{f_s}{f_d} \right)^{3-|3-2\beta|} \left( \frac{f}{f_s} \right)^3, & f \lesssim f_s \end{cases} \quad (2.2)$$

where  $\Omega_{\text{PBB}}$  is the following normalization constant dependent on the radiation density  $\Omega_r$ :

$$\Omega_{\text{PBB}} := \Omega_{r0} H_1^2 \left( \frac{z_\sigma}{z_d} \right)^2, \quad \Omega_{r0} \equiv \Omega_r(\tau_0) \approx 4.15 \times 10^{-5} h^{-2}, \quad (2.3)$$

The range of interest for LISA is the third from the top,  $f_s \lesssim f \lesssim f_d$  [28]. A case of special interest is  $\beta = 0$ , for which the signal is maximized to a plateau. Since  $\Omega_{\text{GW}}(f) \propto f^{3-|3-2\beta|} = f^{3-|3-0|} = f^0 = 1$ , there is no frequency dependence within the observation range for the chosen value of  $\beta$ . As a result, the piecewise function based on simple power laws is not applicable in this scenario and the complete expression must be used instead [28]:

$$\begin{aligned} \Omega_{\text{GW}}(f) &= \Omega_{\text{PBB}} f^3 (f^2 + f_s^2)^{-\frac{|3-2\beta|}{2}} (f^2 + f_d^2)^{-1} (f^2 + f_\sigma^2) (f^2 + f_1^2)^{\frac{|3-2\beta|-3}{2}} \\ &\quad \times \exp\left(-\frac{f}{f_1} + \arctan \frac{f}{f_1}\right) \end{aligned} \quad (2.4)$$

Reducing this equation to the regime of interest ( $f_1 \gg f$ ,  $f_\sigma \gg f$ ), we get the broken power law

$$\Omega_{\text{GW}}(f) = \alpha \frac{f^3}{(f^2 + f_s^2)^{\frac{|3-2\beta|}{2}} (f^2 + f_d^2)}, \quad f_s \lesssim f \lesssim f_d, \quad (2.5)$$

where  $\alpha = \Omega_{\text{PBB}} f_\sigma^2 f_1^{|3-2\beta|-3}$ .

The above characteristic frequencies (in Hz) are functions of the fundamental parameters of the model (appendix A):

$$\begin{aligned} f_1 &\simeq \frac{3.9 \times 10^{11}}{2\pi} H_1^{1/2} m^{1/3} \sigma_i^{-2/3}, & f_\sigma &\simeq \frac{3.9 \times 10^{11}}{2\pi} m^{5/6} \sigma_i^{4/3}, \\ f_d &\simeq \frac{3.9 \times 10^{11}}{2\pi} m^{3/2}, & f_s &= \frac{3.9 \times 10^{11}}{2\pi z_s} H_1^{1/2} m^{1/3} \sigma_i^{-2/3}, \end{aligned} \quad (2.6)$$

where the parameters  $z_s$ ,  $z_\sigma$  and  $z_d$  defined in (2.1) are (appendix A)

$$\begin{aligned} \log_{10} z_s &= \frac{1}{1 - n_s - 2\beta} \left[ \frac{5 - n_s}{2} \log_{10} H_1 - \log_{10} \left( \frac{4.2\pi^2}{\mathcal{T}^2(\sigma_i)} \right) \right. \\ &\quad \left. + 9 - (1 - n_s)(\log_{10} 1.5 - 27) - \frac{n_s - 1}{2} \log_{10} \left( m^{2/3} \sigma_i^{-4/3} \right) \right], \end{aligned} \quad (2.7)$$

$$z_\sigma = H_1^{1/2} m^{-1/2} \sigma_i^{-2}, \quad z_d = H_1^{1/2} m^{-7/6} \sigma_i^{-2/3}. \quad (2.8)$$

Here  $n_s$  is the spectral index of primordial scalar perturbations and  $\mathcal{T}$  is the transfer function [28]. Formula (2.7) follows from the fact that axion perturbations seed curvature perturbations through the curvaton mechanism, in order to match the observed cosmic-microwave-background anisotropies [28]. From the above expressions,  $\Omega_{\text{PBB}}$  can be rewritten as

$$\Omega_{\text{PBB}} = \Omega_{\text{r0}} H_1^2 m^{4/3} \sigma_i^{-8/3}. \quad (2.9)$$

In this work, we parametrize  $\Omega_{\text{GW}}(f)$  (2.5) in terms of  $\beta$  (which describes the high-energy growth of the dilaton and the dynamics of the internal dimensions; it was denoted as  $\beta_h$  in [29]),  $H_1$  (the Hubble parameter when the curvature bounces),  $m$  (the axion mass) and  $\sigma_i$  (the initial axion amplitude after the bounce). This parametrization is chosen for two reasons. First, it is based on the fundamental parameters of the theory and it thus obviates the problem of parameter reconstruction in GW physics, i.e., how to pass from the posterior distributions of the phenomenological parameters used in numerical simulations to the theoretical ones. Second, it allows us to catalogue the effect of each parameter on the GWB curve. For visualization purposes only, a representation of how the variation of each parameter influences the curve is provided in figure 1.

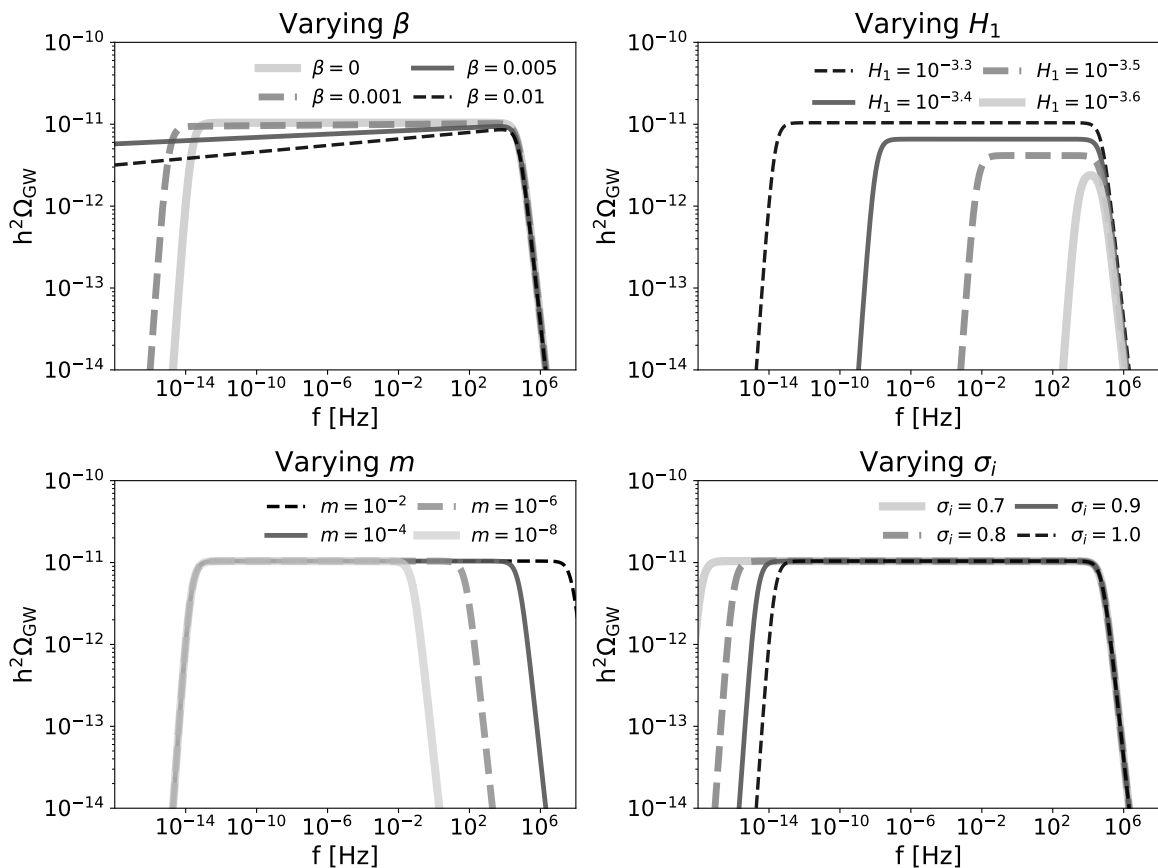


**Figure 1:** Dependence of GWB test curves on the parameters  $\beta$ ,  $H_1$ ,  $m$  and  $\sigma_i$ .

Each parameter affects the signal as follows.

- As the value of  $\beta$  moves further away from 0 to positive values, the left bend of the curve shifts to lower frequencies and the amplitude decreases.

- The smaller the value of  $H_1$ , the more the left bend shifts to higher frequencies and the amplitude decreases.
- The smaller the value of  $m$ , the more the right bend shifts to lower frequencies.
- The smaller the value of  $\sigma_i$ , the more the left bend shifts to lower frequencies.

### 3 Parameter space

As mentioned earlier, the only difference between the minimal and non-minimal scenarios lies in the boundary conditions imposed. Both of them share the following conditions:

- Growing string coupling and avoidance of background instabilities. In the minimal model,

$$0 \leq \beta < 3. \quad (3.1)$$

- Hierarchy of the transition frequency scales:

$$f_s < f_d < f_\sigma \lesssim f_1. \quad (3.2)$$

- The axion background field must be oscillating when it becomes dominant:

$$\log_{10} H_1 + \frac{3}{2} \log_{10} z_d - \frac{7}{2} \log_{10} z_\sigma \leq 0. \quad (3.3)$$

- The end of the the axion dynamics must happen before the big-bang nucleosynthesis scale:

$$\log_{10} H_1 - 3 \log_{10} z_d + \log_{10} z_\sigma > -42 - \log_{10} 4. \quad (3.4)$$

A detailed derivation of these inequalities can be found in [28, 29]. These can be inverted and expressed in terms of the parameters used in this work, yielding the following boundary conditions (appendix B):

$$0 < \beta \leq 3, \quad 10^{-42.6} < H_1 < 1, \quad 10^{-14.2} < m < 1, \quad 10^{-7.1} < \sigma_i < 1. \quad (3.5)$$

As explained in section 2, an extension of the parameter space in the  $\beta < 0$  direction is theoretically possible [29]. This possibility was used to reach the signal detected by the International Pulsar Timing Array (IPTA), which requires  $\Omega_{\text{GW}}(f_s) \approx 2.9_{-2.3}^{+5.4} \times 10^{-8}$ ,  $f_s \approx (1.2 \pm 0.6) \times 10^{-8}$  Hz. In turn, these values are achieved for  $10^{-3} \lesssim H_1 \lesssim 10^{-1}$ ,  $10^{-3/2} \lesssim \sigma_i \lesssim 1$  (both within the range (3.5)) and negative values of  $\beta$  typically of order  $|\beta| = O(10^{-3})$  but up to as low values as  $-0.064$  [29]. The resulting spectrum corresponds to an extreme case, characterized by large amplitude gradients across frequencies.

In the computational part of the present work, we slightly extend the parameter space of the minimal model to include also negative values of  $\beta$  admitted by the non-minimal model. In particular, we set the lower bound for the prior on  $\beta$  to  $-0.05$ . Compared to the  $|\beta| = O(10^{-3})$  values explored in [29], we consider this to be a fairly conservative starting point to explore the parameter space, ensuring that both the minimal and the non-minimal scenario are treated on equal footing. Moreover, all the values of  $H_1$  we explore are significantly larger than  $10^{-10}$ , which is compatible with the fact that  $H_1$  represents the bouncing scale and must be of order of the string mass, independently of the specific scenario considered. We verified

that reducing the lower bound for  $H_1$  to  $10^{-10}$  yields identical results to those obtained by using the full range in (3.5), while improving computational efficiency. On the other hand, we do not explore all the parameter space of the non-minimal model. For instance, we keep  $H_1$  away from 1 and consider injected signals with a medium-to-low amplitude, thus avoiding very-large signals that would drown any other source within the LISA window and produce extreme amplitude gradients towards lower frequencies.

Consequently, the final parameter boundaries adopted in this work consist of a moderate extension of (3.5) to the non-minimal scenario, a shrinking of the range of  $H_1$  and an innocuous rounding of the priors on  $m$  and  $\sigma_i$ :

$$-0.05 < \beta \leq 3, \quad 10^{-10} < H_1 < 1, \quad 10^{-14} < m < 1, \quad 10^{-7} < \sigma_i < 1. \quad (3.6)$$

The density of these priors is uniform for  $\beta$  and  $\sigma_i$  (in the latter case, this is feasible because we inject values at or above 0.2) and log-uniform for  $H_1$  and  $m$ .

## 4 Methodology and results

With the theoretical form of the signal (2.5) and the parameter validity ranges (3.6), we employed the Python package `SGWBinner` [38–40] to determine the posterior distribution of the fundamental parameters of the model given an injected signal and the LISA specifications. We included the noise, the galactic and the extra-galactic foregrounds, letting  $d = 8$  free parameters: four theoretical, two of the noise (low-frequency and high-frequency amplitude) and two of the foregrounds (amplitudes).

We adopted the nested sampling method, in particular, the PolyChord algorithm [41]. For cross-checking, we also used the Markov Chain Monte Carlo (MCMC) method [42, 43], which is implemented within the Cobaya framework [44, 45]. In this work, we only present the results obtained with the first method.

PolyChord uses a cloud of points that is gradually reduced in number as the algorithm converges. It is controlled by three key parameters, the first being the number of live points ( $n_{\text{live}}$ ), which determines the initial size of the point cloud; then, the algorithm calculates the likelihood of each point and converts the ones with the lowest likelihood into dead points. For each dead point, a new live point with higher likelihood is generated by slice sampling, each slice sampling chain having  $n_{\text{repeats}}$  steps. The procedure continues until the uncertainty in the evidence, calculated from both live and dead points, reaches a desired threshold (precision criterion). The parameter configuration used in this work is as follows: number of live points  $80d$  (where  $d = 8$  is the number of free parameters), number of repeats  $2d$  and a precision criterion of  $10^{-5}$ . We checked that the results are robust if we reduce the number of live points to  $60d$  while increasing the number of repeats to  $3d$ .

Regarding the injected signals, we chose four typical cases (figure 2): left-bend feature, right-bend feature and a plateau with high or low signal-to-noise ratio (SNR). We also considered a fifth case with a high-SNR plateau with negative  $\beta = -0.004$  but its results are very similar to the analogous  $\beta = 0$  case. A sixth case, namely of no detection (that can be realized by injecting any signal lying outside the LISA window), is discussed in section 6.

Once the posterior distribution for each parameter in each case has been obtained, two types of information can be extracted: their bounds and their relative uncertainties. Relative uncertainties are

$$\text{Relative uncertainty on } A: \quad \frac{\Delta A}{A_c} = \frac{A_{\text{max}} - A_{\text{min}}}{A_c}, \quad (4.1)$$

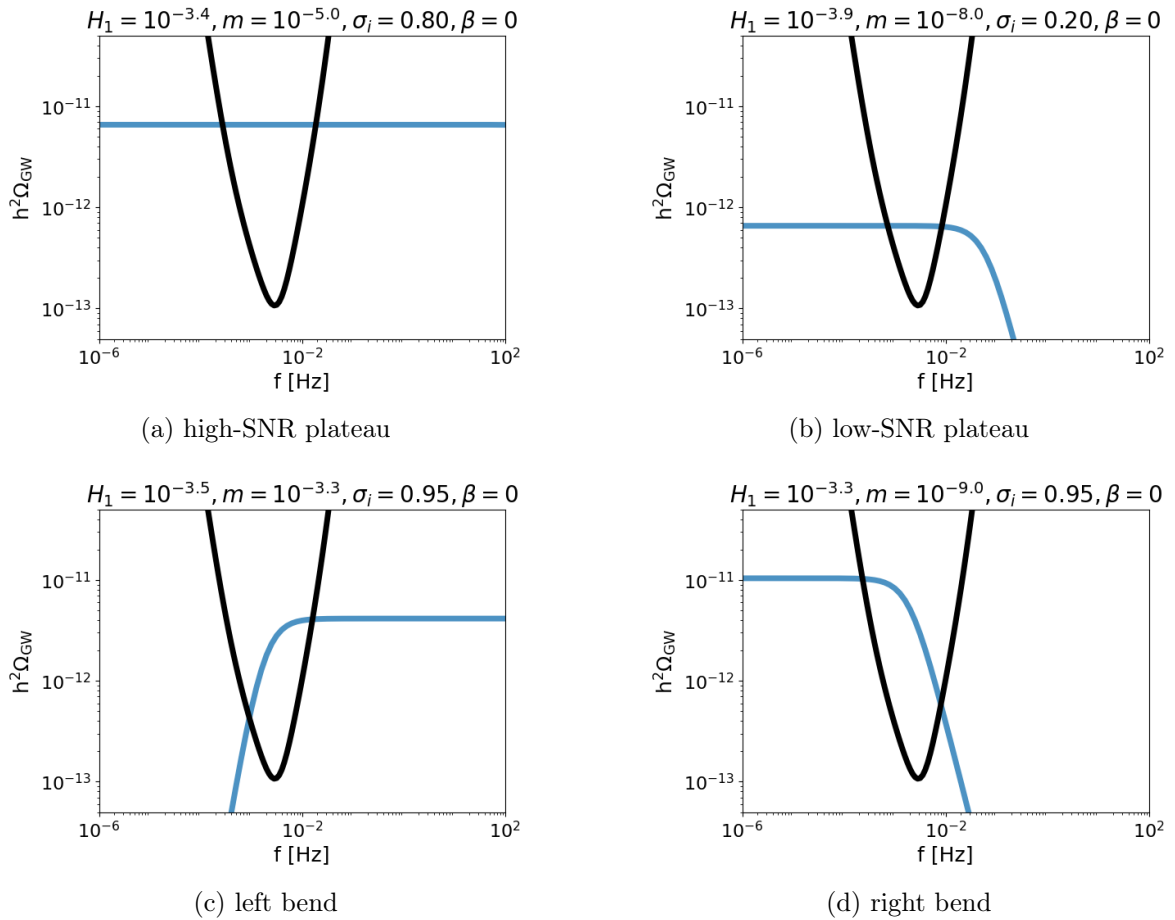


**Figure 2:** The four test curves of the injected signals: a plateau with high SNR (top left); a plateau with low SNR (top right); a left-bend broken power law (bottom left); a right-bend broken power law (bottom right). The LISA sensitivity curve is shown in black and the injected signal in light blue.

where  $A_c \neq 0$  is the injected value of the parameter  $A$  and  $A_{\max}$  and  $A_{\min}$  are the highest and lowest value at a certain confidence level. For parameters such as  $\beta$  where  $A_c = 0$ , the difference  $A_{\max} - A_{\min}$  is considered instead.

The results of the nested sampling analysis performed on the injected signals presented in figure 2 are shown in figures 3–6. Both the galactic and the extra-galactic foregrounds are included.

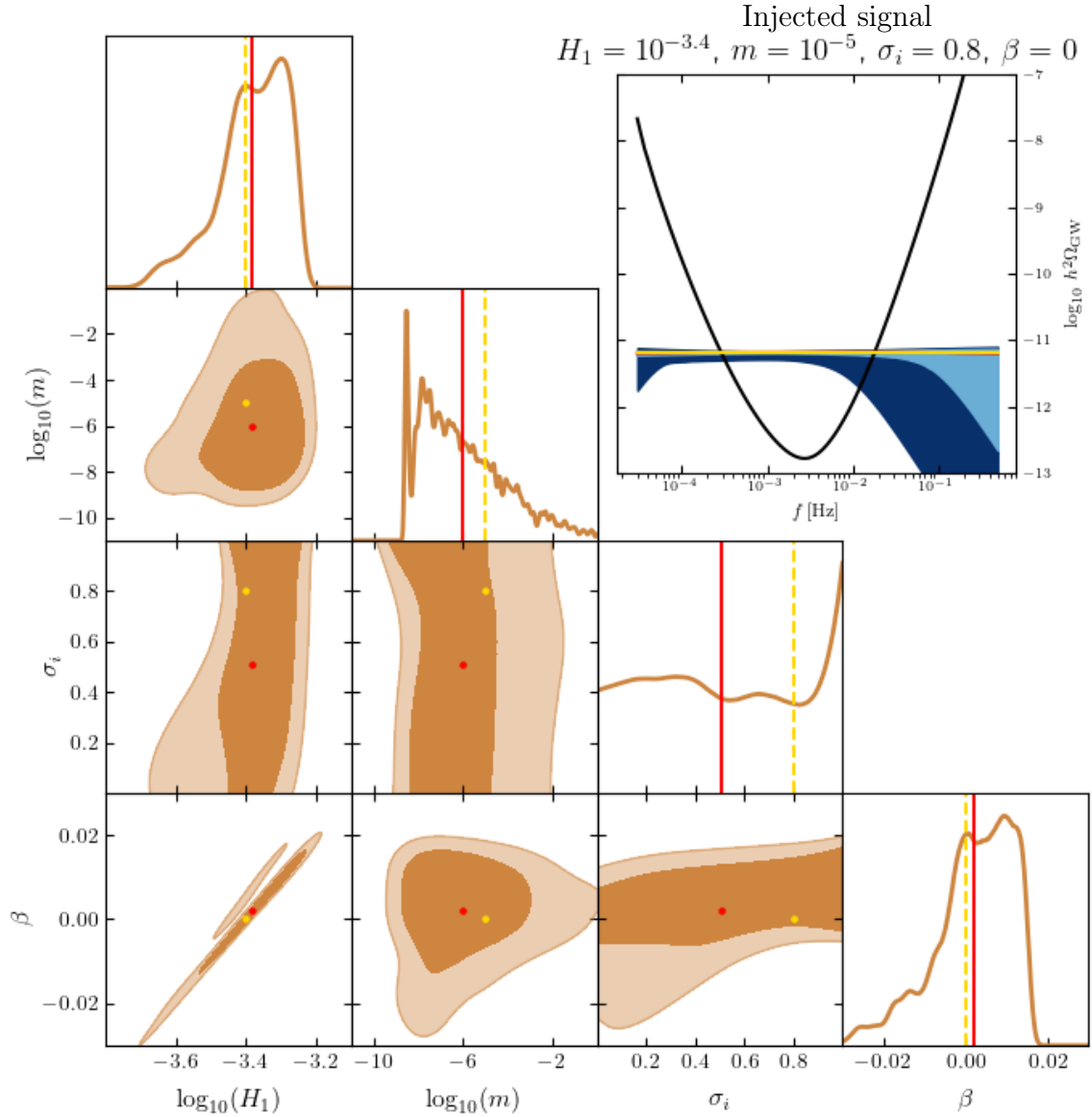


**Figure 3:** Top right: injected test signal of the pre-big-bang scenario (yellow curve) and reconstructed signal (red curve), compared with the LISA sensitivity curve (solid black); shaded regions in light (dark) blue correspond to the 68% (respectively, 95%) CL uncertainty in the reconstructed signal. Triangle plot: Two- and one-dimensional posterior probability distributions of the test-curve parameters. In the marginalized plot, the true and reconstructed value are marked by, respectively, a dashed yellow and a solid red line. The injected values are  $\beta = 0$ ,  $H_1 = 10^{-3.4}$ ,  $m = 10^{-5.0}$  and  $\sigma_i = 0.80$ . Galactic and extra-galactic foregrounds are included.

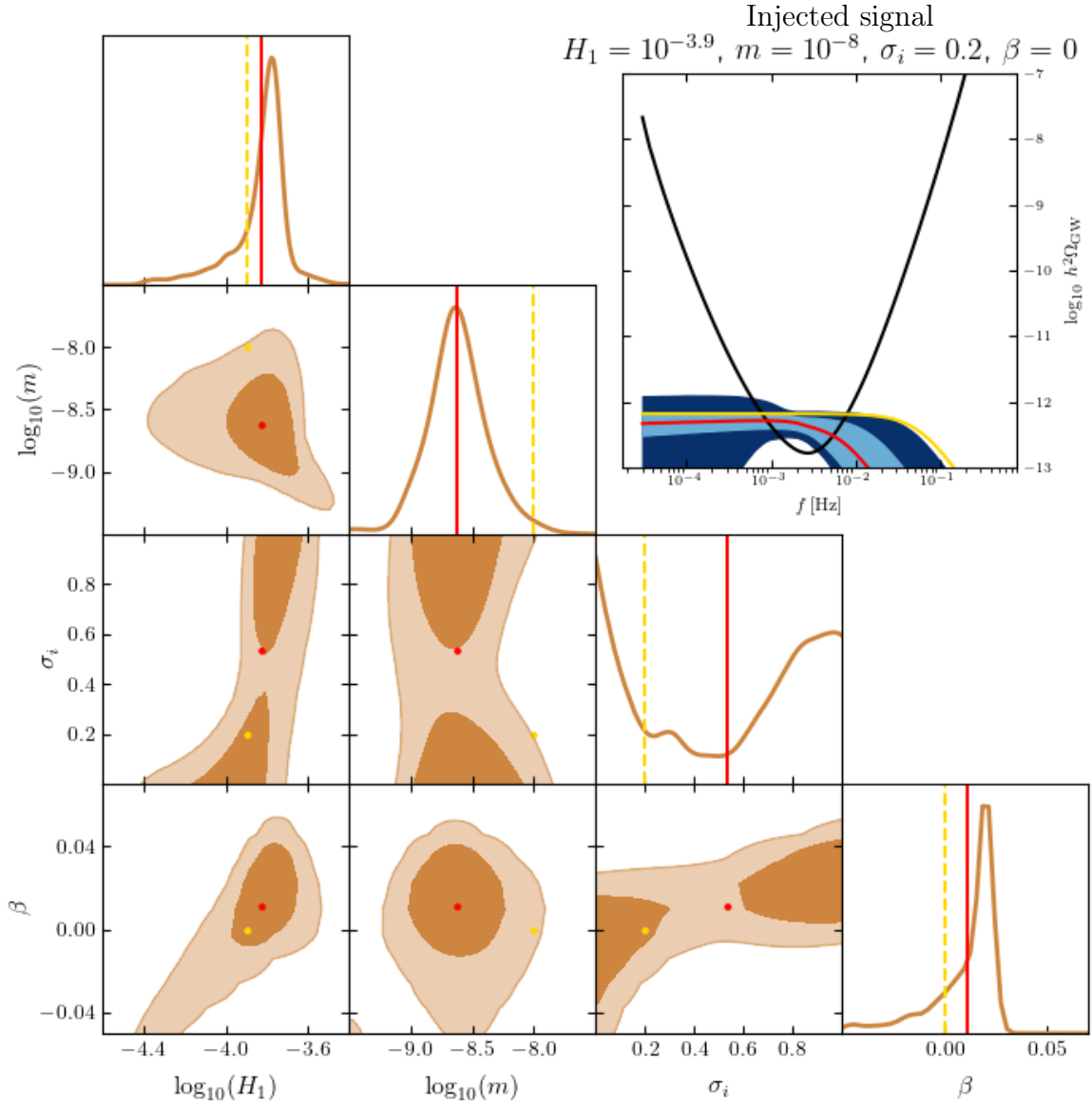


**Figure 4:** Top right: injected test signal of the minimal pre-big-bang scenario (yellow curve) and reconstructed signal (red curve), compared with the LISA sensitivity curve (solid black); shaded regions in light (dark) blue correspond to the 68% (respectively, 95%) CL uncertainty in the reconstructed signal. Triangle plot: Two- and one-dimensional posterior probability distributions of the test-curve parameters. In the marginalized plots, the true and reconstructed values are marked by, respectively, a dashed yellow and a solid red line. The injected values are  $\beta = 0$ ,  $H_1 = 10^{-3.9}$ ,  $m = 10^{-8.0}$  and  $\sigma_i = 0.20$ . Galactic and extra-galactic foregrounds are included.

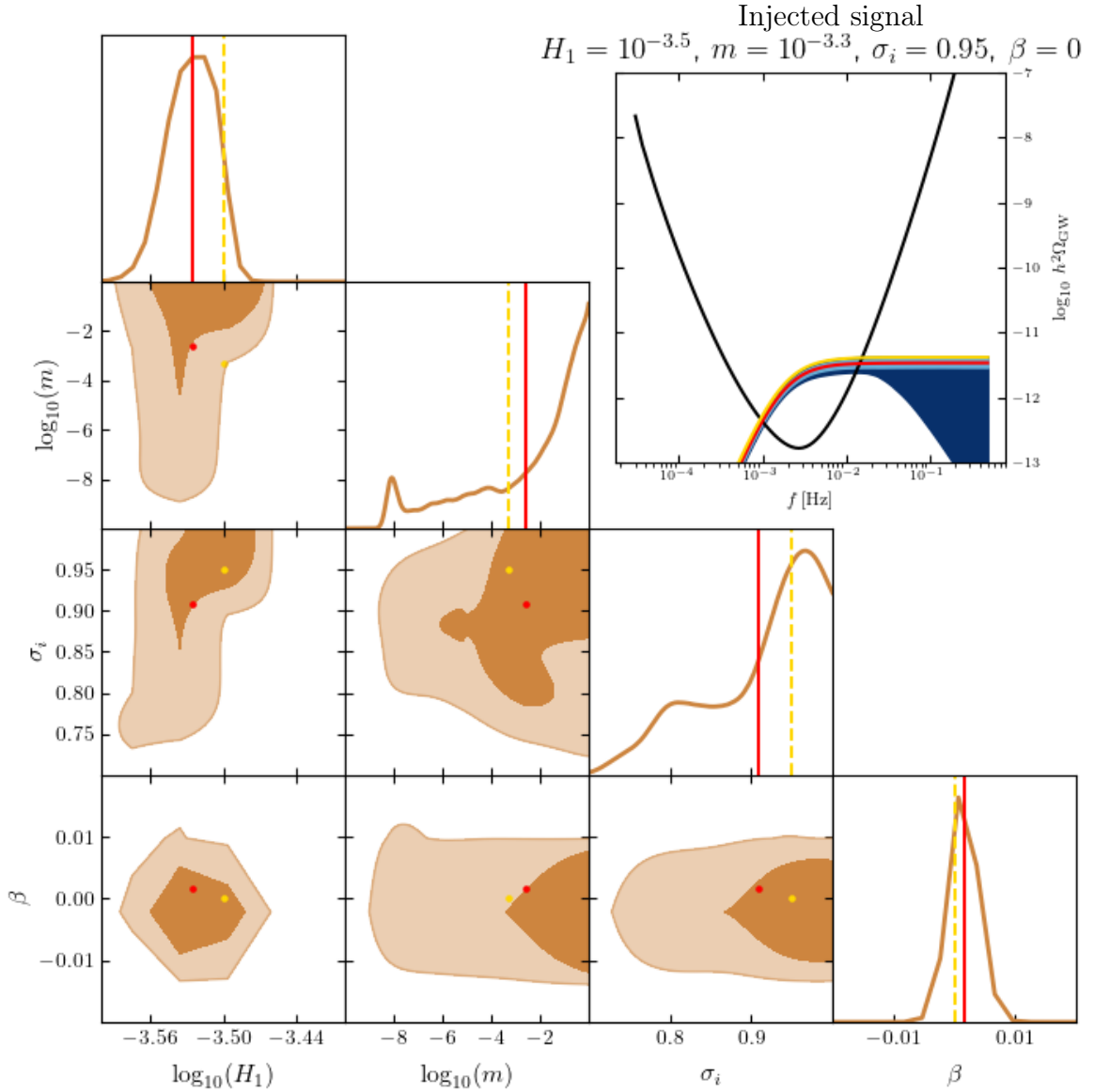


**Figure 5:** Top right: injected test signal of the minimal pre-big-bang scenario (yellow curve) and reconstructed signal (red curve), compared with the LISA sensitivity curve (solid black); shaded regions in light (dark) blue correspond to the 68% (respectively, 95%) CL uncertainty in the reconstructed signal. Triangle plot: Two- and one-dimensional posterior probability distributions of the test-curve parameters. In the marginalized plots, the true and reconstructed values are marked by, respectively, a dashed yellow and a solid red line. The injected values are  $\beta = 0$ ,  $H_1 = 10^{-3.5}$ ,  $m = 10^{-3.3}$  and  $\sigma_i = 0.95$ . Galactic and extra-galactic foregrounds are included.

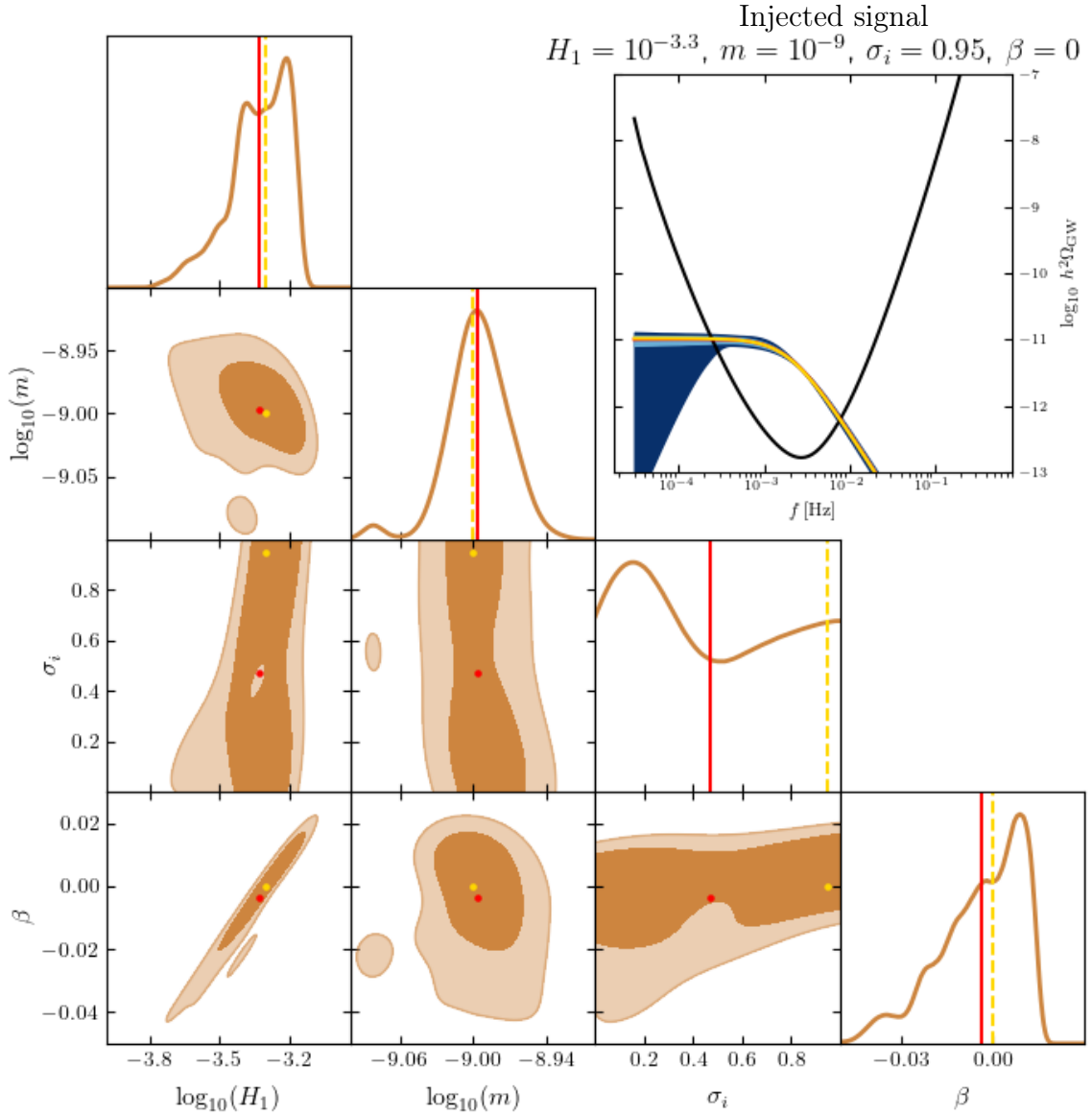


**Figure 6:** Top right: injected test signal of the minimal pre-big-bang scenario (yellow curve) and reconstructed signal (red curve), compared with the LISA sensitivity curve (solid black); shaded regions in light (dark) blue correspond to the 68% (respectively, 95%) CL uncertainty in the reconstructed signal. Triangle plot: Two- and one-dimensional posterior probability distributions of the test-curve parameters. In the marginalized plots, the true and reconstructed values are marked by, respectively, a dashed yellow and a solid red line. The injected values are  $\beta = 0$ ,  $H_1 = 10^{-3.3}$ ,  $m = 10^{-9.0}$  and  $\sigma_i = 0.95$ . Galactic and extra-galactic foregrounds are included.

## 5 Discussion

Let us discuss the bounds and relative uncertainty for each parameter shown in figures 3–6.

- $\beta$ : The lowest precision in the estimation of  $\beta$  occurs for a right-bend configuration, while the highest precision is achieved for the left-bend feature (figure 5). The 95% CL intervals for  $\beta$  can be summarized as follows:  $|\beta| < 0.011$  in the case of a left bend (figure 5);  $|\beta| < 0.022$  for a plateau with high SNR (figure 3);  $|\beta| < 0.045$  for a plateau with low SNR (figure 4);  $-0.04 < \beta < 0.02$  in the case of a right bend (figure 6). This behaviour is consistent with the fact that variations in  $\beta$  induce a slope on the low-frequency side of the curve, as illustrated in figure 1. Therefore, if the signal displays a right bend, then the value of  $\beta$  becomes less relevant, whereas for a left bend it plays a more critical role.
- $H_1$ : focusing now on the subplots depicting  $\beta$  vs.  $\log_{10} H_1$ , it is possible to estimate the relative uncertainty on  $H_1$ . From figures 3–6, the relative uncertainties at 68% CL are approximately 62%, 135%, 18% and 63%, respectively. The variation in uncertainties can be explained by the fact that when the left bend lies far from the detection curve or the amplitude is low, the uncertainty  $\Delta H_1$  increases, due to the behaviour shown in figure 1. Therefore, the left bend (figure 5) is characterized by a more accurate estimation of  $H_1$  compared to when one has a plateau or a right bend. In other words, there is a degeneracy of the effect of  $H_1$  and  $\beta$  unless one observes a left bend.
- $m$ : in the cases of a high-SNR plateau and a left bend (respectively, figure 3 and 5), at 95% CL no upper bound smaller than the Planck mass can be set. The lower bound of  $10^{-8}$  is due to the signal becoming undetectable below this value. Therefore, if LISA detected a plateau or a left-bend feature, no constraints could be placed on  $m$ . However, if the degeneracy was broken by choosing a value of  $m$  that results in a right-bend feature in the LISA window (figure 6), then the relative uncertainty would drop to  $\Delta m/m \approx 18\%$  at 68% CL. Figure 4 (low-SNR plateau) shows an upper bound on this parameter that occurs because the mean of the posteriors (red curve) fails to reconstruct accurately the position of the right bend in the injected signal (yellow curve) and places such bend within the LISA sensitivity curve, despite this not being the intended behaviour of the injected signal. Therefore, constraints of this type should be analyzed with extra care when the SNR is low.
- $\sigma_i$ : for a left-bend feature (figure 5),  $\sigma_i > 0.85$  at 68% CL. If a high-SNR plateau or a right-bend feature were present (respectively, figure 3 and 6), then no constraints could be set, since  $\sigma_i$  would not affect the signal amplitude within the explorable region. If a low-amplitude plateau was detected (figure 4), then  $\sigma_i$  would be minimally constrained: the likelihood distribution changes from roughly uniform over the entire prior range to having a higher probability for values below 0.4 and above 0.6. This type of bimodal distribution is typical of low-SNR signals.

## 6 Conclusions

Regarding the four parameters that characterize the GWB in this model, the following conclusions can be drawn:

- For the parameter  $\beta$ , the best constraints are obtained when the signal exhibits a left-bend feature, followed by the plateau shape for both high and low SNR cases. The poorest constraint is found in the right-bend scenario.
- Concerning  $H_1$ , the smallest relative uncertainty is achieved when the left-bend lies within the LISA sensitivity curve, in which case the relative uncertainty is  $\Delta H_1/H_1 \approx 18\%$ . However, if the left bend lies far from the sensitivity region, then the relative uncertainty can increase up to 63%. Furthermore, if the left bend lies far from the sensitivity region and the signal amplitude is low, then the relative uncertainty can exceed 100%, thus making this parameter indeterminable.
- For  $m$ , due to its degeneracy with other parameters, constraints can only be placed when the right bend lies within the sensitivity window, reaching a relative uncertainty of about  $\Delta m/m \approx 18\%$  at 68% CL.
- Regarding  $\sigma_i$ , a similar situation occurs but in the opposite direction: it can only be constrained when the left bend falls within the sensitivity range, reaching a relative uncertainty of approximately  $\Delta \sigma_i/\sigma_i \approx 12\%$  at 68% CL.

These results are physically meaningful, as both  $H_1$  and  $\sigma_i$  govern the behaviour of the left bend and meaningful constraints are obtained when the signal displays such a feature. The same applies to  $\beta$ , which determines the position of the left bend and, additionally, the slope of the curve.  $m$  follows a similar trend but for the right bend.

To conclude, based on the analysis carried out, we find that LISA will be capable of placing significant constraints on the parameter space of the considered model, especially for the mass  $m$  and the exponent  $\beta$ ; the relative error on  $H_1$  and  $\sigma_i$  is comparatively larger depending on the injected signal.

Should a power-law or a broken-power-law signal be observed, the pre-big-bang scenario would emerge as an appealing candidate to explain the data. This alone would not confirm the model itself, since there may be other early-universe models producing a similar signal at those frequencies and amplitudes. Nevertheless, in case this degeneracy were removed in favour of the pre-big-bang model (e.g., by polarization or multi-band observations spanning also cosmic-microwave-background scales), the implications for cosmology would be groundbreaking: not only would a detection suggest that general relativity requires an extension to the quantum realm but it would also provide a first empirical evidence supporting string theory.

Conversely, in the lack of detection all the parameters  $H_1$ ,  $m$ ,  $\sigma_i$  and  $\beta$  would remain completely undetermined. This result, which we checked numerically, is somewhat obvious for  $\sigma_i$  and  $\beta$  (since lower values of  $0 < \sigma_i < 1$  only shift the left bend to lower frequencies and  $\beta$  only modifies the slope of the  $\beta = 0$  plateau without affecting the global maximum value of the amplitude) but less so for  $H_1$  and  $m$ . This inability to constrain the pre-big-bang model, if no GWB signal consistent with its predictions were observed within the LISA sensitivity range, is a typical case of “over-parametrization,” where the number of free parameters does not allow to extract predictions in the case of no detection. Such a case might motivate the development of alternative experimental strategies to overcome the limitations that prevented LISA from detecting the signal, for instance, by looking at multi-band measurements involving frequency ranges where the model has a foothold, such as in the band covered by the Einstein Telescope [28].

## Acknowledgments

G.C. is supported by grant PID2020-118159GB-C41 funded by the Spanish Ministry of Science, Innovation and Universities MCIN/AEI/10.13039/501100011033. We warmly thank M. Pieroni and J. Torrado for invaluable discussions and support in the implementation, execution and problem-solving of the `SGWBinner`. We also thank J.A. Rubiño and C. Perdomo for their helpful corrections and suggestions on an early version of this work as part of X.V.C.'s MSc thesis, as well as M. Gasperini, E. Pavone, R. Rosati and, again, M. Pieroni and J. Torrado for detailed feedback on a first draft of the manuscript.

## A Derivation of (2.6)

Let us start with  $f_1$  [28, eq. (B.6)]:

$$f_1 = \frac{3.9 \times 10^{11}}{2\pi} \left( \frac{H_1}{M_{\text{Pl}}} \right)^{1/2} \left( \frac{z_\sigma}{z_d} \right)^{1/2},$$

where here and in the following we omit the Hz units. To evaluate this expression, one must refer to eq. (4.9) of the same paper to obtain the values of  $z_\sigma$  and  $z_d$ :

$$\begin{aligned} z_\sigma &\simeq \left( \frac{H_1}{M_{\text{Pl}}} \right)^{1/2} \left( \frac{m}{M_{\text{Pl}}} \right)^{-1/2} \left( \frac{\sigma_i}{M_{\text{Pl}}} \right)^{-2} \stackrel{M_{\text{Pl}}=1}{=} H_1^{1/2} m^{-1/2} \sigma_i^{-2}, \\ z_d &= z_\sigma m^{-2/3} \sigma_i^{4/3} = H_1^{1/2} m^{(-4-3)/6} \sigma_i^{(-6+4)/3} = H_1^{1/2} m^{-7/6} \sigma_i^{-2/3}. \end{aligned}$$

Then,

$$\frac{z_\sigma}{z_d} = m^{(-3+7)/6} \sigma_i^{(-6+2)/3} = m^{2/3} \sigma_i^{-4/3},$$

so that

$$f_1 = \frac{3.9 \times 10^{11}}{2\pi} H_1^{1/2} m^{1/3} \sigma_i^{-2/3}. \quad (\text{A.1})$$

Regarding  $f_\sigma$ , using once again [28, eq. (4.9)], we get  $f_\sigma = f_1/z_\sigma$  and

$$f_\sigma = \frac{3.9 \times 10^{11}}{2\pi} m^{5/6} \sigma_i^{4/3}. \quad (\text{A.2})$$

Following the same process for  $f_d$ , we obtain  $f_d = f_\sigma z_\sigma/z_d$  and

$$f_d = \frac{3.9 \times 10^{11}}{2\pi} m^{3/2}. \quad (\text{A.3})$$

Last,  $f_s$  can be obtained from its definition [28, eq. (4.8g)]:

$$f_s = \frac{f_1}{z_s} = \frac{3.9 \times 10^{11}}{2\pi z_s} H_1^{1/2} m^{1/3} \sigma_i^{-2/3}. \quad (\text{A.4})$$

## B Derivation of (3.5)

In this appendix, we manipulate eqs. (3.2)–(3.4) to extract the prior bounds on the fundamental theoretical parameters of the model. Let us begin by rewriting (3.3) as a function of the parameters  $H_1$ ,  $m$  and  $\sigma_i$  (in  $M_{\text{Pl}} = 1$  units):

$$\log_{10} H_1 + \frac{3}{2} \log_{10} \left( H_1^{1/2} m^{-7/6} \sigma_i^{-2/3} \right) - \frac{7}{2} \log_{10} \left( H_1^{1/2} m^{-1/2} \sigma_i^{-2} \right) \leq 0$$

Thus, the factors in  $H_1$  and  $m$  cancel out, yielding  $\log_{10} \sigma_i \leq 0$  and

$$\sigma_i \leq 1. \quad (\text{B.1})$$

Next, we rewrite (3.4):

$$\log_{10} H_1 - 3 \log_{10} \left( H_1^{1/2} m^{-7/6} \sigma_i^{-2/3} \right) + \log_{10} \left( H_1^{1/2} m^{-1/2} \sigma_i^{-2} \right) > -42 - \log_{10} 4 \approx -42.6$$

The factors of  $H_1$  and  $\sigma_i$  cancel out:

$$3 \log_{10} m > -42.6 \quad \implies \quad m > 10^{-14.2}. \quad (\text{B.2})$$

From (3.2),

$$f_\sigma > f_d \quad \implies \quad \frac{3.9 \times 10^{11}}{2\pi} m^{5/6} \sigma_i^{4/3} > \frac{3.9 \times 10^{11}}{2\pi} m^{3/2},$$

and solving for  $m$  we obtain

$$m^{3/2-5/6} = m^{2/3} < \sigma_i^{4/3} \quad \implies \quad m < \sigma_i^2. \quad (\text{B.3})$$

Another condition from (3.2) is

$$f_1 \gtrsim f_\sigma \quad \implies \quad H_1^{1/2} m^{1/3} \sigma_i^{-2/3} \gtrsim m^{5/6} \sigma_i^{4/3}.$$

Solving for  $H_1$ ,

$$H_1 \gtrsim m \sigma_i^4, \quad (\text{B.4})$$

and by substituting the value obtained in (B.1) into (B.3) we have

$$m < 1. \quad (\text{B.5})$$

The final upper bound for  $H_1$  can be derived by recalling that the kinematic details of the bounce are expected to affect only the very-high-frequency modes that cross the horizon during the bounce phase itself. For further details, see [24]. Hence,

$$H_1 < 1. \quad (\text{B.6})$$

A similar procedure can be applied to the lower bounds by substituting the value from (B.2) into (B.3):

$$\sigma_i > 10^{-14.2/2} = 10^{-7.1}, \quad (\text{B.7})$$

and introducing both values into (B.4) we get

$$H_1 \gtrsim 10^{-14.2} \times 10^{-7.1 \times 4} = 10^{-42.6}. \quad (\text{B.8})$$

## References

- [1] B.P. Abbott et al. [LIGO Scientific and VIRGO Collaborations], *Observation of gravitational waves from a binary black hole merger*, *Phys. Rev. Lett.* **116** (2016) 061102 [[arXiv:1602.03837](#)].
- [2] A.G. Abac et al. [LIGO Scientific, VIRGO and KAGRA Collaborations], *GWTC-4.0: Updating the gravitational-wave transient catalog with observations from the first part of the fourth LIGO-Virgo-KAGRA Observing Run*, [arXiv:2508.18082](#).
- [3] A.G. Abac et al. [LIGO Scientific, VIRGO and KAGRA Collaborations], *GWTC-4.0: Population properties of merging compact binaries*, [arXiv:2508.18083](#).
- [4] B.P. Abbott et al. [LIGO Scientific and VIRGO Collaborations], *Tests of general relativity with GW150914*, *Phys. Rev. Lett.* **116** (2016) 221101; *Erratum-Ibid.* **121** (2018) 129902 [[arXiv:1602.03841](#)].
- [5] R. Abbott et al. [LIGO Scientific, VIRGO and KAGRA], *Tests of general relativity with GWTC-3*, [arXiv:2112.06861](#).
- [6] LIGO Scientific and VIRGO Collaboration, *GW230814: Investigation of a loud gravitational-wave signal observed with a single detector*, [arXiv:2509.07348](#).
- [7] A.G. Abac et al. [LIGO Scientific, VIRGO and KAGRA Collaborations], *GW250114: Testing Hawking's area law and the Kerr nature of black holes*, *Phys. Rev. Lett.* **135** (2025) 111403 [[arXiv:2509.08054](#)].
- [8] M. Maggiore et al., *Science case for the Einstein Telescope*, *JCAP* **2003** (2020) 050 [[arXiv:1912.02622](#)].
- [9] P.Amaro-Seoane. et al. [LISA Astrophysics Working Group], *Astrophysics with the Laser Interferometer Space Antenna*, *Living Rev. Relativ.* **26** (2023) 2 [[arXiv:2203.06016](#)].
- [10] P. Auclair et al. [LISA Cosmology Working Group], *Cosmology with the Laser Interferometer Space Antenna*, *Living Rev. Relativ.* **26** (2023) 5 [[arXiv:2204.05434](#)].
- [11] K.G. Arun et al. [LISA Fundamental Physics Working Group], *New horizons for fundamental physics with LISA*, *Living Rev. Relat.* **25** (2022) 4 [[arXiv:2205.01597](#)].
- [12] M. Colpi et al., *LISA definition study report*, [arXiv:2402.07571](#).
- [13] A. Abac et al. *The science of the Einstein Telescope*, [arXiv:2503.12263](#).
- [14] N. Christensen, *Stochastic gravitational wave backgrounds*, *Rept. Prog. Phys.* **82** (2019) 016903 [[arXiv:1811.08797](#)].
- [15] A.I. Renzini, B. Goncharov, A.C. Jenkins and P.M. Meyers, *Stochastic gravitational-wave backgrounds: current detection efforts and future prospects*, *Galaxies* **10** (2022) 34 [[arXiv:2202.00178](#)].
- [16] N. van Remortel, K. Janssens and K. Turbang, *Stochastic gravitational wave background: methods and implications*, *Prog. Part. Nucl. Phys.* **128** (2023) 104003 [[arXiv:2210.00761](#)].
- [17] D. Oriti (ed.), *Approaches to quantum gravity*, Cambridge University Press, Cambridge, U.K. (2009).
- [18] G.F.R. Ellis, J. Murugan and A. Weltman (eds.), *Foundations of space and time*, Cambridge University Press, Cambridge, U.K. (2012).
- [19] C. Bambi, L. Modesto and I.L. Shapiro (eds.), *Handbook of Quantum Gravity*, Springer, Singapore (2024).
- [20] M. Gasperini and G. Veneziano, *Pre-big bang in string cosmology*, *Astropart. Phys.* **1** (1993) 317 [[arXiv:hep-th/9211021](#)].

- [21] M. Gasperini and G. Veneziano, *The pre-big bang scenario in string cosmology*, *Phys. Rept.* **373** (2003) 1 [[arXiv:hep-th/0207130](#)].
- [22] M. Gasperini and G. Veneziano, *String theory and pre-big bang cosmology*, *Nuovo Cim. C* **38** (2016) 160 [[arXiv:hep-th/0703055](#)].
- [23] M. Gasperini, *Elements of String Cosmology*, Cambridge University Press, Cambridge, U.K. (2007).
- [24] M. Gasperini, *Observable gravitational waves in pre-big bang cosmology: an update*, *JCAP* **12** (2016) 010 [[arXiv:1606.07889](#)].
- [25] M. Gasperini, *From pre- to post-big bang: an (almost) self-dual cosmological history*, *Phil. Trans. Roy. Soc. Lond. A* **380** (2022) 20210179 [[arXiv:2106.12865](#)].
- [26] M. Gasperini and G. Veneziano, *Non-singular pre-big bang scenarios from all-order  $\alpha'$  corrections*, *JHEP* **07** (2023) 144 [[arXiv:2305.00222](#)].
- [27] P. Conzino, G. Fanizza, M. Gasperini, E. Pavone, L. Tedesco and G. Veneziano, *From the string vacuum to FLRW or de Sitter via  $\alpha'$  corrections*, *JCAP* **12** (2023) 019 [[arXiv:2308.16076](#)].
- [28] I. Ben-Dayan, G. Calcagni, M. Gasperini, A. Mazumdar, E. Pavone, U. Thattarampilly and A. Verma, *Gravitational-wave background in bouncing models from semi-classical, quantum and string gravity*, *JCAP* **09** (2024) 058 [[arXiv:2406.13521](#)].
- [29] P. Conzino, G. Fanizza, M. Gasperini, E. Pavone, L. Tedesco and G. Veneziano, *Constraints on the Pre-Big Bang scenario from a cosmological interpretation of the NANOGrav data*, *JCAP* **02** (2025) 039 [[arXiv:2412.01734](#)].
- [30] P. Conzino, M. Gasperini and E. Pavone, *A simple example of “non-minimal” pre-big bang scenario*, [[arXiv:2506.00995](#)].
- [31] G. Veneziano, *Scale factor duality for classical and quantum strings*, *Phys. Lett. B* **265** (1991) 287.
- [32] G. Agazie et al. [NANOGrav], *The NANOGrav 15-year data set: evidence for a gravitational-wave background*, *Astrophys. J. Lett.* **951** (2023) L8 [[arXiv:2306.16213](#)].
- [33] A. Afzal et al. [NANOGrav], *The NANOGrav 15 yr data set: search for signals from new physics*, *Astrophys. J. Lett.* **951** (2023) L11 [[arXiv:2306.16219](#)].
- [34] J. Antoniadis et al., *The second data release from the European Pulsar Timing Array III. Search for gravitational wave signals*, *Astron. Astrophys.* **678** (2023) A50 [[arXiv:2306.16214](#)].
- [35] D.J. Reardon et al. [PPTA], *Search for an isotropic gravitational-wave background with the Parkes Pulsar Timing Array*, *Astrophys. J. Lett.* **951** (2023) L6 [[arXiv:2306.16215](#)].
- [36] H. Xu et al. [CPTA], *Searching for the nano-Hertz stochastic gravitational wave background with the Chinese Pulsar Timing Array Data Release I*, *Res. Astron. Astrophys.* **23** (2023) 075024 [[arXiv:2306.16216](#)].
- [37] G. Agazie et al. [International Pulsar Timing Array], *Comparing recent PTA results on the nanohertz stochastic gravitational wave background*, *Astrophys. J.* **966** (2024) 105 [[arXiv:2309.00693](#)].
- [38] C. Caprini, D.G. Figueroa, R. Flauger, G. Nardini, M. Peloso, M. Pieroni, A. Ricciardone and G. Tasinato, *Reconstructing the spectral shape of a stochastic gravitational wave background with LISA*, *JCAP* **11** (2019) 017 [[arXiv:1906.09244](#)].
- [39] M. Pieroni and E. Barausse, *Foreground cleaning and template-free stochastic background extraction for LISA*, *JCAP* **07** (2020) 021; *Erratum-Ibid.* **09** (2020) E01 [[arXiv:2004.01135](#)].
- [40] R. Flauger, N. Karnesis, G. Nardini, M. Pieroni, A. Ricciardone and J. Torrado, *Improved reconstruction of a stochastic gravitational wave background with LISA*, *JCAP* **01** (2021) 059 [[arXiv:2009.11845](#)].

- [41] W.J. Handley, M.P. Hobson and A.N. Lasenby, *Polychord: next-generation nested sampling*, *MNRAS* **453** (2015) 4385.
- [42] A. Lewis and S. Bridle, *Cosmological parameters from CMB and other data: A Monte Carlo approach*, *Phys. Rev.* **D66** (2002) 103511 [[arXiv:astro-ph/0205436](#)].
- [43] A. Lewis, *Efficient sampling of fast and slow cosmological parameters*, *Phys. Rev.* **D87** (2013) 103529 [[arXiv:1304.4473](#)].
- [44] J. Torrado and A. Lewis, *Cobaya: Code for Bayesian Analysis of hierarchical physical models*, *JCAP* **05** (2021) 057 [[arXiv:2005.05290](#)].
- [45] J. Torrado and A. Lewis, *Cobaya: Bayesian analysis in cosmology*, Astrophysics Source Code Library, [record ascl:1910.019](#) (2019).